

Effect on drag of the flow orientation at the base separation of a simplified blunt road vehicle

M. Grandemange · A. Mary · M. Gohlke · O. Cadot

Received: date / Accepted: date

Abstract The separated flow past the square-back model used in the experiments of Ahmed *et al.* [1] is controlled using flaps at the end of the top and bottom faces. A parametric study of the flow regarding the slant angle of the flaps is performed from pressure and force measurements as well as particle image velocimetry (PIV). When the bottom flap orientation is fixed, variations of the top slant angle evidence a drag versus lift quadratic dependence. This relationship presents self similarities changing the bottom flap angle. It is then observed that the lift is an affine function of both slant angles and the force a second order polynomial containing a coupling term between the two angles. These drag evolutions varying both angles are discussed and interpreted as contributions of the wake size, a drag induced by the lift and a local drag induced by the inclination of the flaps.

Keywords Flow control · Drag reduction · Induced drag · Ahmed geometry

M. Grandemange
Unité de Mécanique, Ecole Nationale Supérieure de Techniques Avancées, ParisTech, Chemin de la Hunière, 91761 Palaiseau Cedex, France
PSA Peugeot Citroën, Centre Technique de Velizy, Route de Gisy, 78943 Vélizy-Villacoublay Cedex, France
E-mail: mathieu.grandemange@ensta-paristech.fr

A. Mary · M. Gohlke
PSA Peugeot Citroën, Centre Technique de Velizy, Route de Gisy, 78943 Vélizy-Villacoublay Cedex, France

O. Cadot
Unité de Mécanique, Ecole Nationale Supérieure de Techniques Avancées, ParisTech, Chemin de la Hunière, 91761 Palaiseau Cedex, France

1 Introduction

Many industrial flows are related to the motion of bluff bodies in a fluid; the bluntness associated with the functional shape provokes flow separations on the afterbody and consequently complex wake dynamics. Over the past three decades, growing issues on energy have motivated research activities to improve the understanding of the wake past basic geometries. The objective is then often to limit unwanted aerodynamic effects such as drag or vibrations through optimization of the geometry or flow control.

In the case of the automotive aerodynamics, the work of Ahmed *et al.* [1] describes the effect of the afterbody shape of a vehicle on the flow topology and on the drag. Their work proves the critical influence of the slant angle of the rear window on a simplified road vehicle. The drag plotted versus the slant angle up to 30° presents parabolic shape with a minimum drag reduction of 8% for a slant inclination of 12.5° . Over this optimal value the drag increases continuously; the worst case (slant angle close to 30°) is associated with a 50% increase in drag in comparison to the 0° case. Over a critical angle close to 30° , the drag decreases abruptly to recover values close to the 0° configuration. In terms of flow topologies, the blunt afterbody is responsible for a massive separation on the base. For slant angles less than 30° , the flow remains attached on the rear window (at least partially) and then a pair of counter-rotating vortices develops from the sides of the slanted face [2]: the intensity of these streamwise vortices gradually grows in parallel with the drag increase. Over 30° , the flow separates upstream of the rear window, a massive recirculation region without energetic streamwise vortices, similar to the 0° case, is recovered.

The geometry used in the experiments of Ahmed *et al.* [1] is massively used to explore drag reduction strategies needed by industry. Thus, literature reports the use of various different control devices. Much work has been devoted to the 25° slant angle configuration; significant drag reductions are achieved through passive or active control strategies such as splitter plates [3], flaps [4, 5], boundary layer streaks [6] or even pulsed jets [7]. Diverse strategies equally provide interesting base pressure recovery in the square-back case: splitter plates [8], porous devices [9] or active control [10].

The recent experiments of Littlewood & Passmore [11] depict the effect of a small chamfer at the upper trailing edge of a square-back geometry. The geometry of the afterbody is similar to the 0° Ahmed configuration. Despite its small size in the streamwise direction (only 15% of the base height), an optimal drag reduction of 4.4% is obtained for a chamfer angle of 12° . The parabolic-like dependence between the chamfer angle and the drag is reminiscent of the results of Ahmed *et al.* [1] for moderate slant angles where an optimal 8% drag reduction is obtained for a 12.5° . Thus, the significant drag reduction obtained by Littlewood & Passmore [11] with a small chamfer highlights the high sensitivity of the flow to its orientation at the trailing edge.

This approach using chamfered shapes is particularly interesting since it corresponds to the method applied by the car manufacturers on real vehicles to limit the drag. Indeed, the angles of the spoiler and of the diffuser (when one is present) are set empirically to reach the optimum drag point given the vehicle parameters (global shape, ground clearance...), the characteristic length of these devices remaining small compared to the vehicle size.

The present work clarifies the link between the angles of the trailing edge, the flow topologies and the aerodynamic forces. The objective is to provide a comprehensive analysis to the method commonly used during the development of real cars that has not been provided in literature yet. In particular, the coupling effect between the angles of the separations from the top and bottom faces is evidenced and discussed.

The article is organized as follows. In Sec. 2, the experimental setup and measurements are presented. Then, Sec. 3 is devoted to the results which are discussed in Sec. 4. Eventually, the concluding remarks are presented in Sec. 5.

2 Experimental set-up

The studied bluff body is the square-back model used in the experiments of Ahmed *et al.* [1]. The flow is con-

trolled by two flaps mounted downstream of the top and bottom faces of the model as depicted in Fig. 1(a). The streamwise length of the flaps is 50 mm, their crossflow length matches the width of the geometry and their thickness is 2 mm. The slant angles of the flaps can be controlled in the range $(\phi_T, \phi_B) \in [-12^\circ, 17^\circ] \times [-17^\circ, 12^\circ]$; these ranges remain reasonably small to keep the flow attached on the flaps in all the configurations. The slant inclination of the flaps is set with a precision better than 1° . The different angle couples studied are presented in Fig. 1(b).

The coordinate system is defined as x in the streamwise direction, z normal to the ground and y forming a direct trihedral. The origin of the coordinate system is in the reflectional plane of symmetry on the ground at the position of the base in the x direction.

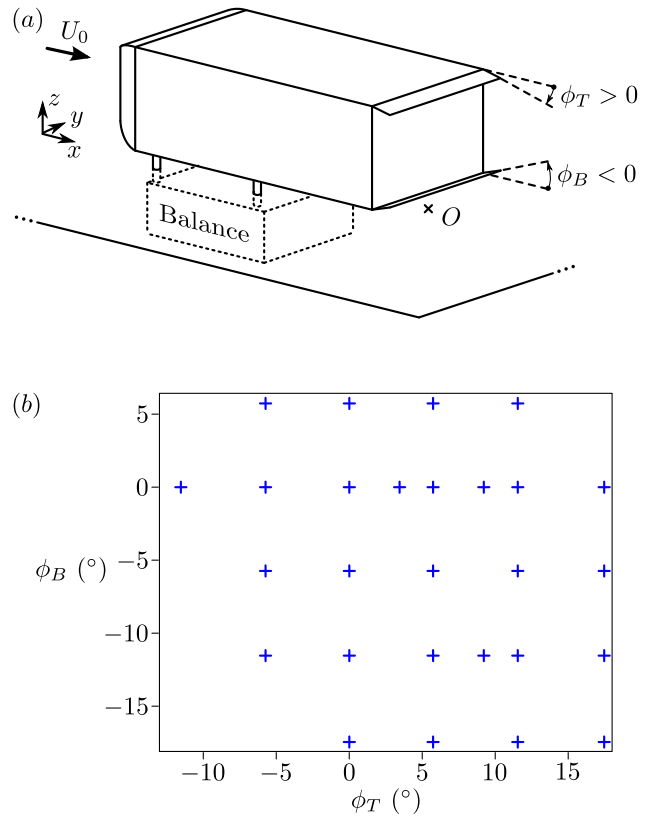


Fig. 1 (a) Experimental set-up of the model; O sets the origin of the coordinate system; dihedral angles ϕ_T and ϕ_B are displayed positive and negative respectively. (b) Couples of slant angles (ϕ_T, ϕ_B) studied.

The experiments are performed in the PSA in-house wind tunnel used in the experiments of Beaudoin and Aider [4] or Pujals *et al.* [6]. This facility is an open wind tunnel with a 6 m long test section and a rectangular cross-section 2.1 m high and 5.2 m wide. The

turbulence intensity is 1.3%. The main flow velocity is $U_0 = 40 \text{ m s}^{-1}$ and the Reynolds number based on the height of the base of the geometry ($\text{Re} = U_0 H / \nu$) is $7.4 \cdot 10^5$. The velocities are defined as $\mathbf{u} = u_x \mathbf{e}_x + u_y \mathbf{e}_y + u_z \mathbf{e}_z$; u_{ij} is the amplitude of velocity at the considered point in the plane $(\mathbf{e}_i, \mathbf{e}_j)$. $A = \langle a \rangle$ is the time-averaged value of any quantity a . The height of the base H , density ρ and inlet velocity U_0 are used to obtain non-dimensional values marked with an asterisk. For example, the dimensionless mean vorticity is denoted $\boldsymbol{\Omega}^* = \mathbf{rot} \mathbf{U} H / U_0$.

Drag and lift, denoted respectively F_x and F_z , are obtained using a strain balance. The dimensionless coefficient C_i of the aerodynamic force in the i direction is defined according to Eq. (1) using $S = 0.118 \text{ m}^2$ the projected area of the geometry in a cross-flow plane.

$$C_i = \frac{F_i}{\frac{1}{2} \rho S U_0^2}, \quad (1)$$

with $i \in \{x, z\}$. Each measurement consists in five samples of 60 s at the frequency of 50 Hz. The precision in the measurement of C_x and C_z are 0.001 and 0.002 respectively.

The pressure on the body is measured at 47 locations around the entire geometry in the reflectional plane of symmetry. The levels of pressure are analyzed through the dimensionless pressure coefficient defined as:

$$C_p = \frac{P - P_0}{\frac{1}{2} \rho U_0^2}. \quad (2)$$

The pressure measurement is based on the time-averaged value obtained with one sample of 60 s; the precision is better than 4 Pa. To locate the taps in the plane $y^* = 0$, the curvilinear abscissa s is used; its origin is taken in the middle of the base and goes positive on the top face.

In addition, a wake analysis is made from Particle Image Velocimetry (PIV) measurements. The system is comprised of a Quantal Big Sky Laser (dual pulse Nd:YAG) and a DANTEC CCD cameras (FlowSense MkII, 4 Mpx). The set-up acquires image pairs at a rate of 10 Hz; each acquisition records 400 image pairs. The interrogation window size is 32×32 pixels with an overlap of 75%. The mean velocities are taken into account only when more than 80% of the 400 measurements are valid vectors. Note that the flaps are transparent which enable the PIV measurement close to the base.

3 Results

In this section, the force measurements, pressure levels on the geometry and flow topologies are depicted varying the top and bottom slant angles. First, the effect of the top flap orientation ϕ_T in the case $\phi_B = 0^\circ$ is considered in Sec. 3.1. Then, the analyses are extended to the different bottom slant angles in Sec. 3.2. Finally, the drag and lift are presented in the bi-dimensional domain (ϕ_T, ϕ_B) in Sec. 3.3.

3.1 Study of the $\phi_B = 0^\circ$ cases

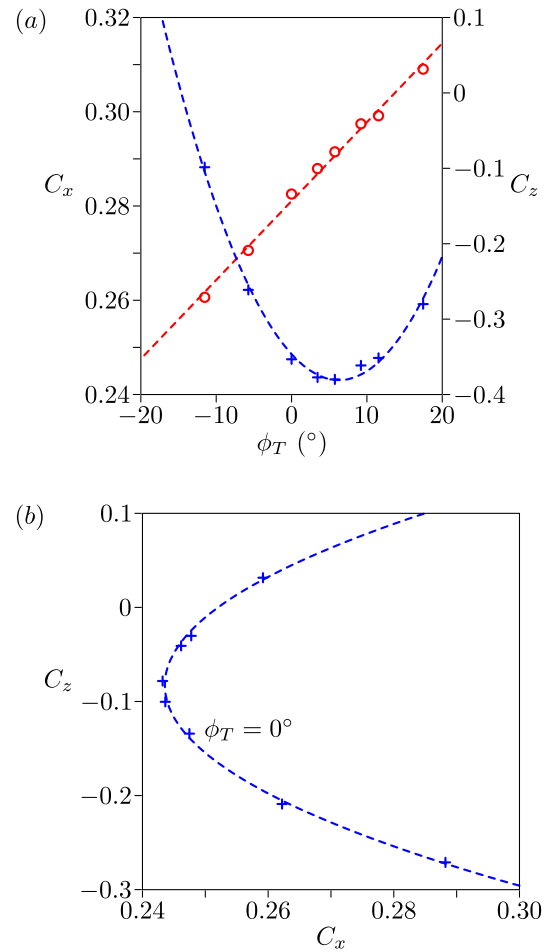


Fig. 2 (a) Drag (+) and lift (O) as a function of the top slant angle ϕ_T for $\phi_B = 0^\circ$; ---, 1st and 2nd order polynomial fit for drag and lift respectively. (b) Drag versus lift as a parametric function of the top slant angle ϕ_T for $\phi_B = 0^\circ$: +, experimental data; ---, 2nd order polynomial fit.

First, the inclination of the bottom flap is fixed at $\phi_B = 0^\circ$. The results of the drag and lift coefficients associated with the different top flap angles are pre-

sented in Fig. 2(a). As reported by Littlewood & Passmore [11], the lift is an affine function of the top flap inclination. It can be fitted by:

$$C_z = 0.600 \phi_T - 0.143, \quad (3)$$

with ϕ_T in radians.

On the other hand, the drag presents a minimum for $\phi_T = 6^\circ$ with a 1.8% reduction in comparison to the case $(\phi_T, \phi_B) = (0^\circ, 0^\circ)$. The experimental data follows a 2nd order polynomial fit given by:

$$C_x = 0.243 + 0.457 (\phi_T - 0.110)^2, \quad (4)$$

with ϕ_T in radians.

Similar parabolic-like dependences toward ϕ_T for the drag are presented in the experiments of Ahmed *et al.* [1] and Littlewood & Passmore [11]. From these results, a clear quadratic dependence between the drag and the lift is reported. The relationship plotted in Fig. 2(b) is given by:

$$C_x = 0.244 + 1.242 (C_z + 0.083)^2. \quad (5)$$

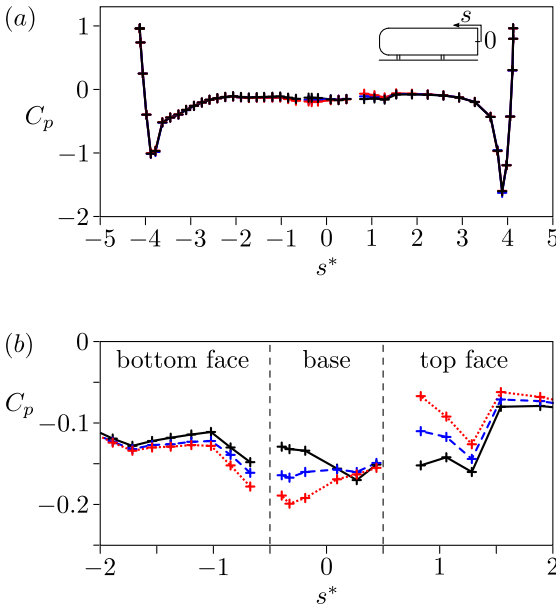


Fig. 3 Pressure distribution in the plane $y^* = 0$ around the entire geometry (a) and focused on the afterbody (b) for $\phi_B = 0^\circ$ with different ϕ_T : —, $\phi_T = 6^\circ$; ---, $\phi_T = 0^\circ$; ···, $\phi_T = -6^\circ$.

These force evolutions are associated with changes of the wall pressure distribution on the model which are presented in Fig. 3. The effect of the flaps on the pressure is limited to the after-body (see Fig. 3a). Therefore, the affine dependence between the lift and ϕ_T (Eq. 3) as well as the quadratic relationship between the drag and the lift (Eq. 5) remain valid when the rear

lift is considered instead of the global lift; depending on the measurement facilities, it may give more accurate results.

Focusing on the afterbody, the effect of the inclination of the top flap is displayed in Fig. 3(b). The angle of the top flap significantly affects the pressure on the top face before separation as well as the base pressure distribution (especially the base pressure gradient in the z direction). Slight variations in the pressure levels on the bottom face are also observed. These levels of pressure are consistent with the classification of the configuration in terms of drag and lift. These evolutions of pressure levels correspond to modifications of the flow topologies around the afterbody.

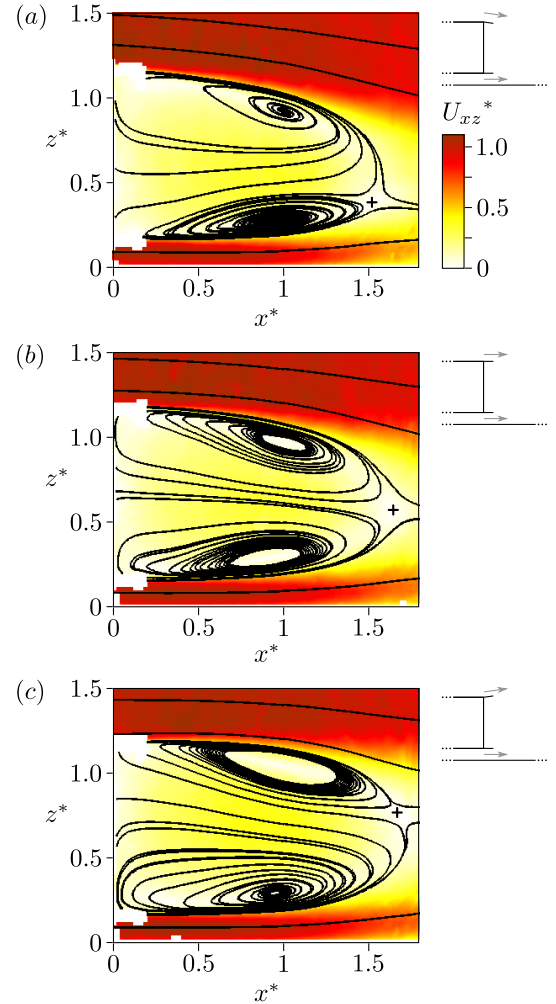


Fig. 4 Velocity measurements in the plane $y^* = 0$ for $\phi_T = 6^\circ$ (a), $\phi_T = 0^\circ$ (b) and $\phi_T = -6^\circ$ (c) with $\phi_B = 0^\circ$; crosses are saddle points.

The velocity measurements in the plane $y^* = 0$ are presented in Fig. 4. The configurations correspond to

the cases studied in Fig. 3 through the pressure distributions ($\phi_T = 6^\circ, 0^\circ$ and -6° with $\phi_B = 0^\circ$). The change of the top slant angle then induces differences in the flows organization around the recirculation bubble. First, the angle of the top flap affects the streamline orientation in the flow over the body. For $\phi_T = 6^\circ$ (see Fig. 4a), the flow separates at the end of the flap following the slant inclination. Moreover, the orientation of the flap induces changes in the streamline direction even upstream of the separation and up to $z^* = 1.5$. The results are similar for $\phi_T = 0^\circ$ and $\phi_T = -6^\circ$ (see Figs. 4b-c); despite its small length, the flap is able to orient the potential flow before the separation on the top face. On the contrary, the direction of the streamlines from the under-body flow remains unchanged. These observations are consistent with the differences in the pressure levels on the afterbody. In particular, the classification of the streamline curvature before separation on the top face is directly linked to the classification of pressure levels visible in Fig. 3(b). As the inclination of the flow before separation is affected by the top flap angle ϕ_T , the height of the wake after the end of the recirculation is strongly modified and the length of the recirculation region is slightly affected.

The direction of the backward flow in the middle of the recirculation region ($x^* \approx 0.8, z^* \approx 0.6$) is equally changed which may be confronted to the base pressure gradient in the z direction visible in Fig. 3(b). The lowest pressure on the base is measured at the opposite side of the mean backward flow: for example, the flow presented in Fig. 4(a) presents a backward flow oriented toward the ground and then the pressure gradient in the z direction on the base is negative (see Fig. 3b). Such an association between an asymmetry in the recirculation bubble and a base pressure gradient is equally observed in Grandemange *et al.* [12]. On the contrary, the centers of the averaged recirculation structures remain at first order at the same location; what changes is the relative position of the saddle point at the end of the recirculation: it is centered for $\phi_T = 0^\circ$ whereas it goes close to the upper recirculation structure for $\phi_T = -6^\circ$ and to the lower one for $\phi_T = 6^\circ$.

The optimal drag configuration for $\phi_B = 0^\circ$ is measured at $\phi_T = 6^\circ$, the velocities and pressure measurements show that this case do not correspond to the best top / bottom symmetry of the recirculation region: the saddle point at the end of the recirculation closure is off-centered (see Fig. 4a) and the base pressure gradient in the z direction is clearly negative (see Fig. 3b) in comparison to the $\phi_T = 0^\circ$ case.

As a result, the flow is highly sensitive to the top flap angle in the case $\phi_B = 0^\circ$ because it controls the top /

bottom equilibrium of the recirculation region as well as the wake height. The influence of the bottom flap angle on the previous results is now considered in Sec. 3.2.

3.2 Study varying ϕ_T at different ϕ_B

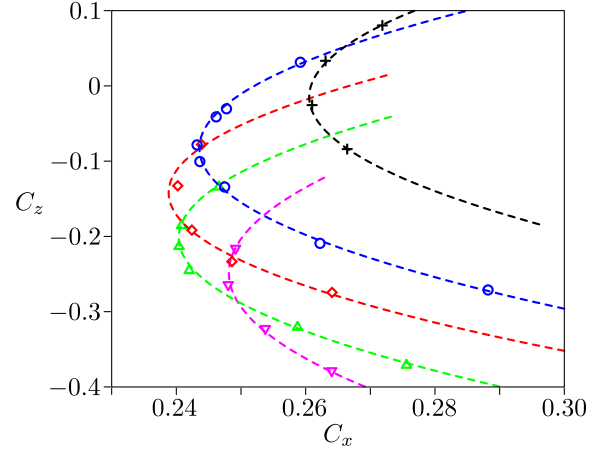


Fig. 5 Drag versus lift as a parametric function of the top slant angle ϕ_T : +, $\phi_B = 6^\circ$; O, $\phi_B = 0^\circ$; \diamond , $\phi_B = -6^\circ$; \triangle , $\phi_B = -12^\circ$; ∇ , $\phi_B = -17^\circ$; ---, 2nd order polynomial fits.

The dependences between the lift and the drag for different values of the bottom flap angle ϕ_B varying the top flap angle ϕ_T are plotted in Fig. 5. For each value of ϕ_B , a quadratic relation is found between C_x and C_z ; the results are similar to the $\phi_B = 0^\circ$ case presented in Sec. 3.1. Thus, as presented in Eq. (5), the data varying ϕ_B at constant ϕ_T follows:

$$C_x = C_{x0} + \alpha (C_z - C_{z0})^2, \quad (6)$$

with C_{x0} , C_{z0} and α the three parameters defining the 2nd order polynomial fit.

Figure 6 presents the data centered on their respective value of C_{x0} and C_{z0} . For all the values of ϕ_B , the data points superimpose well on the master curve:

$$C_x - C_{x0} = \alpha (C_z - C_{z0})^2, \quad (7)$$

with $\alpha = 1.25$. Therefore, the curves shown in Fig. 5 are identical and α is independent of the angle of the bottom flap ϕ_B . The relationship between the lift and the drag are then perfectly defined from the two parameters C_{x0} and C_{z0} . Besides, it is observed that the optimal top flap angle ϕ_T is a function of the bottom flap angle ϕ_B indicating that the optimal drag configuration results from a coupling between the two angles and not from independent optimization regarding ϕ_T and ϕ_B .

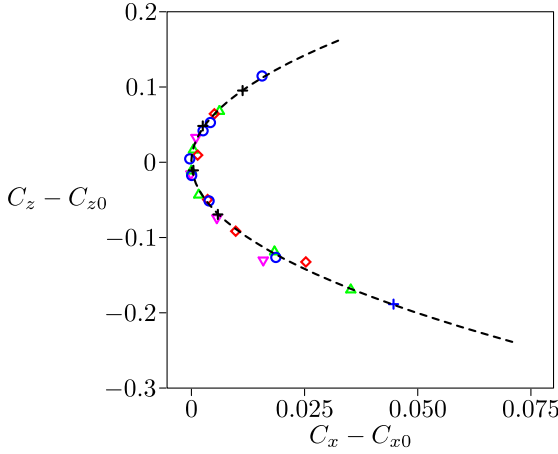


Fig. 6 Drag versus lift for different values of ϕ_B centered on their respective value of C_{x0} and C_{z0} : +, $\phi_B = 6^\circ$; \circ , $\phi_B = 0^\circ$; \diamond , $\phi_B = -6^\circ$; \triangle , $\phi_B = -12^\circ$; ∇ , $\phi_B = -17^\circ$; ---, 2nd order polynomial fit of all the centered data.

The relationship between the forces of the optimal points C_{x0} and C_{z0} associated with the different values of ϕ_B is now studied. Figure 7(a) displays the dependence between ϕ_B and C_{z0} . The optimal lift linearly depends on the bottom slant angle according to:

$$C_{z0} = 0.580 \phi_B - 0.079, \quad (8)$$

with ϕ_B in radians.

On the other hand, the optimal drag presents C_{x0} a quadratic evolution referring to C_{z0} given by:

$$C_{x0} - C_{x\text{opt}} = \beta (C_{z0} - C_{z\text{opt}})^2, \quad (9)$$

with $\beta = 1.14$, $C_{x\text{opt}} = 0.238$ and $C_{z\text{opt}} = -0.155$. This relationship can be seen in Fig. 7(b). $C_{x\text{opt}}$ is then the optimal drag point considering both parameters ϕ_T and ϕ_B ; $C_{z\text{opt}}$ is the associated lift. This optimal configuration corresponds to the flap angles $\phi_{T\text{opt}} = 9.2^\circ$ and $\phi_{B\text{opt}} = -7.4^\circ$.

Experimentally, the best configuration in terms of drag is obtained for the case ($\phi_T = 12^\circ$, $\phi_B = -6^\circ$) with $C_x = 0.240$ and $C_z = -0.133$. The associated drag and the corresponding flap angles are relatively close to $C_{x\text{opt}}$ and ($\phi_{T\text{opt}}$, $\phi_{B\text{opt}}$) given the precision of the force measurement and the limited resolution of the parameters ϕ_T and ϕ_B in the experiments (see Fig. 1b). The corresponding velocity field is presented in Fig. 8. The flow respects a certain top / bottom symmetry of the recirculation structures since the mean backward flow is mostly oriented along x and the saddle point is centered in the z direction at the end of the recirculation. The wake height is strongly reduced in comparison with the one associated with the case $\phi_T = \phi_B = 0^\circ$ presented in Fig. 4(b); the recirculation length in the streamwise direction is also decreased.

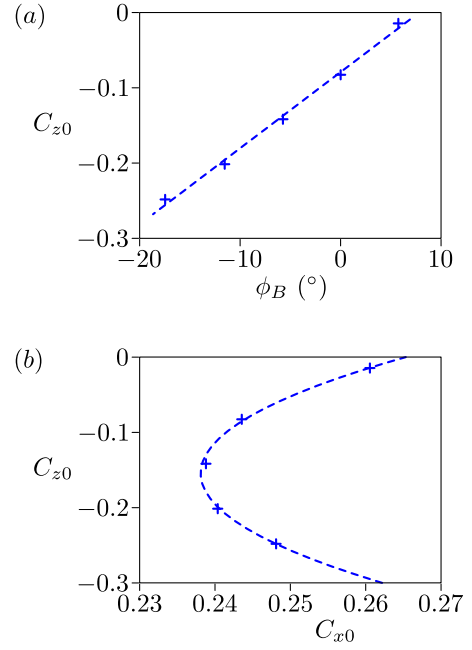


Fig. 7 (a) C_{z0} as a function of the bottom slant angle $\phi_B = 0^\circ$: +, experimental data; ---, 1st order polynomial fit. (b) C_{x0} versus C_{z0} as a parametric function of the bottom slant angle $\phi_B = 0^\circ$: +, experimental data; ---, 2nd order polynomial fit.

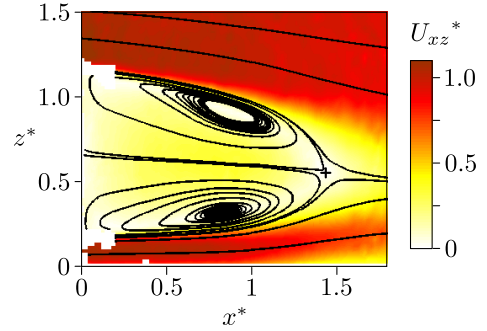


Fig. 8 Velocity measurements in the plane $y^* = 0$ for $\phi_T = 12^\circ$ and $\phi_B = -6^\circ$; cross is saddle point.

However, it is worth noting that neither the wake height nor the recirculation region length are the only parameters of order of the drag. Indeed, the case $\phi_T = 12^\circ$ and $\phi_B = -17^\circ$ (optimal top angle for $\phi_B = -17^\circ$) presents a thinner wake and a shortened recirculation region (see Fig. 9) but it still presents a larger drag coefficient ($C_x = 0.248$). Therefore, past a certain point, when the slant angles are oriented further toward the recirculation region, the wake height keeps decreasing but the drag increases because of three-dimensional effects.

The inclination of the flaps leads to pressure differences between the top (or bottom) face and the side

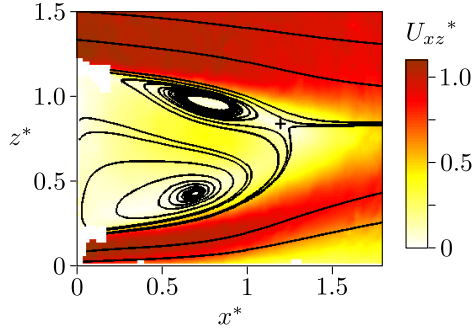


Fig. 9 Velocity measurements in the plane $y^* = 0$ for $\phi_T = 12^\circ$ and $\phi_B = -17^\circ$; cross is saddle point.

faces upstream of the base (see Fig. 3b). As a result, streamwise vortices develop from the lateral edges of the flaps. Such structures, already suggested in the results of Littlewood & Passmore [11] must then be responsible for part of the drag [13].

To evidence this point, contours of streamwise vorticity in the plane $x^* = 0.6$ are presented in Fig. 10 for different configurations: $(\phi_T = 0^\circ, \phi_B = 0^\circ)$, $(\phi_T = 12^\circ, \phi_B = 6^\circ)$ and $(\phi_T = 12^\circ, \phi_B = -12^\circ)$. In the case $(\phi_T = 0^\circ, \phi_B = 0^\circ)$ presented in Fig. 10(a), there are no signs of vortices; however, as soon as the flaps are inclined (see Figs. 10b–c), strong vortices are measured in the near wake downstream of the side edges of the flaps; the sign of the vorticity depends on the flap orientation. When the signs of ϕ_T and ϕ_B are identical, the vortices from the one side of the model ($y^* > 0$ or $y^* < 0$) are co-rotating (see Fig. 10b) whereas, when the signs are different, the vortices are counter-rotating (see Fig. 10c).

As the height of the body is smaller than its width, the vortices from one side of the geometry are sufficiently close to interact further downstream in the wake. Contours of streamwise vorticity in the plane $x^* = 2.0$ are presented in Fig. 11 for same three configurations: $(\phi_T = 0^\circ, \phi_B = 0^\circ)$, $(\phi_T = 12^\circ, \phi_B = 6^\circ)$ and $(\phi_T = 12^\circ, \phi_B = -12^\circ)$. Like in the near wake, there is no significant vorticity in the case $(\phi_T = 0^\circ, \phi_B = 0^\circ)$ (see Fig. 11a) but very different structures are reported depending on whether the vortices from one side of the geometry co-rotate or counter-rotate. In the configuration $(\phi_T = 12^\circ, \phi_B = 6^\circ)$ (see Fig. 11b), the pairs of co-rotating vortices from the sides of the model ($y^* > 0$ and $y^* < 0$) merge which lead to two strong counter-rotating vortices. In the case $(\phi_T = 12^\circ, \phi_B = -12^\circ)$ presented in Fig. 11c, the pairs counter-rotating vortices have a destructive contribution to the streamwise vorticity; as a result, moving downstream, the vortices

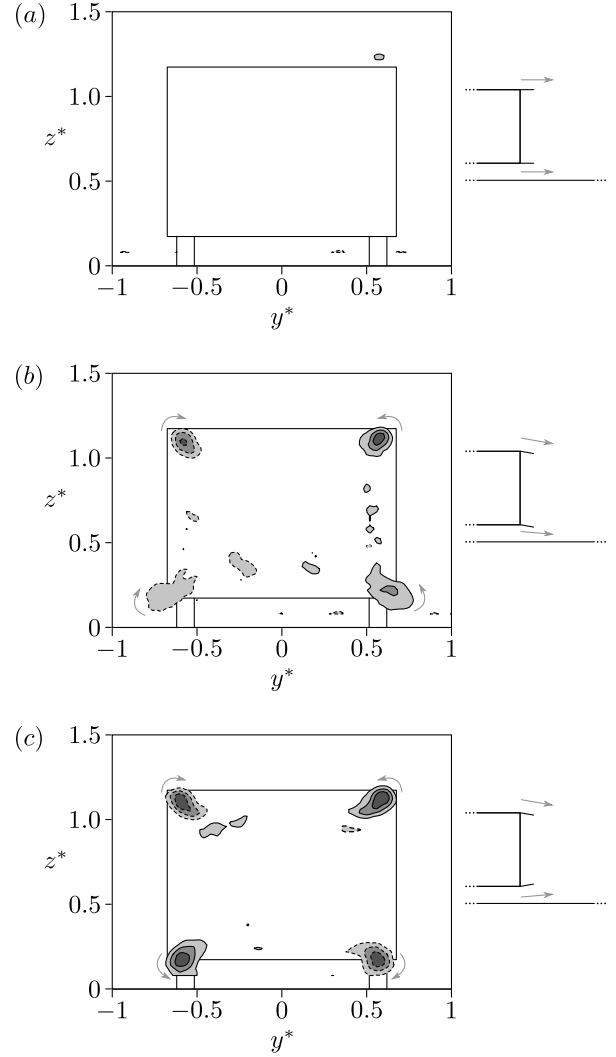


Fig. 10 Contours of streamwise vorticity Ω_{x^*} in the plane $x^* = 0.6$ for $(\phi_T = 0^\circ, \phi_B = 0^\circ)$ (a), $(\phi_T = 12^\circ, \phi_B = 6^\circ)$ (b) and $(\phi_T = 12^\circ, \phi_B = -12^\circ)$ (c). Continuous and dashed lines are respectively positive and negative values, contour intervals are 2, contour 0 is not plotted.

gradually lose their intensity.

3.3 Study in the domain (ϕ_T, ϕ_B)

To go further in the analyses, the measurements of lift and drag are considered in the bi-dimensional domain (ϕ_T, ϕ_B) . The experimental lift as a function of the angles ϕ_T and ϕ_B is displayed in Fig. 12(a). The affine dependence toward the top slant angle depicted in Fig. 2 for the case $\phi_B = 0^\circ$ is confirmed for all the values of ϕ_B . Besides, Fig. 12(a) proves that the lift is equally an

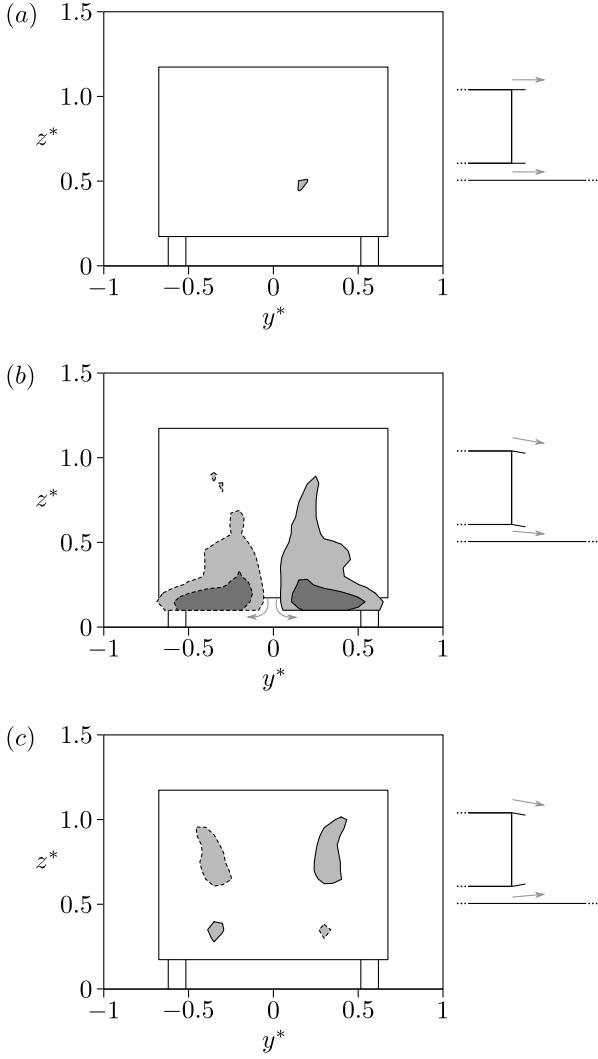


Fig. 11 Contours of streamwise vorticity Ω_x^* in the plane $x^* = 2.0$ for $(\phi_T = 0^\circ, \phi_B = 0^\circ)$ (a), $(\phi_T = 12^\circ, \phi_B = 6^\circ)$ (b) and $(\phi_T = 12^\circ, \phi_B = -12^\circ)$ (c). Continuous and dashed lines are respectively positive and negative values, contour intervals are 2, contour 0 is not plotted.

affine function of ϕ_B for all the values of ϕ_T . Thus, it can be fitted by:

$$C_z = -0.135 + 0.566 \phi_T + 0.858 \phi_B, \quad (10)$$

with ϕ_T and ϕ_B in radians. The affine fit given in Eq. (10) is shown in Fig. 12(b).

Like the lift, the drag can be plotted in the domain (ϕ_T, ϕ_B) . The results displayed in Fig. 13(a) confirms the presence of the minimal drag configuration for $(\phi_T \approx 10^\circ, \phi_B \approx -10^\circ)$ presented in Sec. 3.2. In addition, the quadratic evolution of the drag regarding ϕ_T (see Sec. 3.1) is recovered and a similar dependence toward ϕ_B is observed.

Besides, the results detailed in Sec. 3.2, in particular

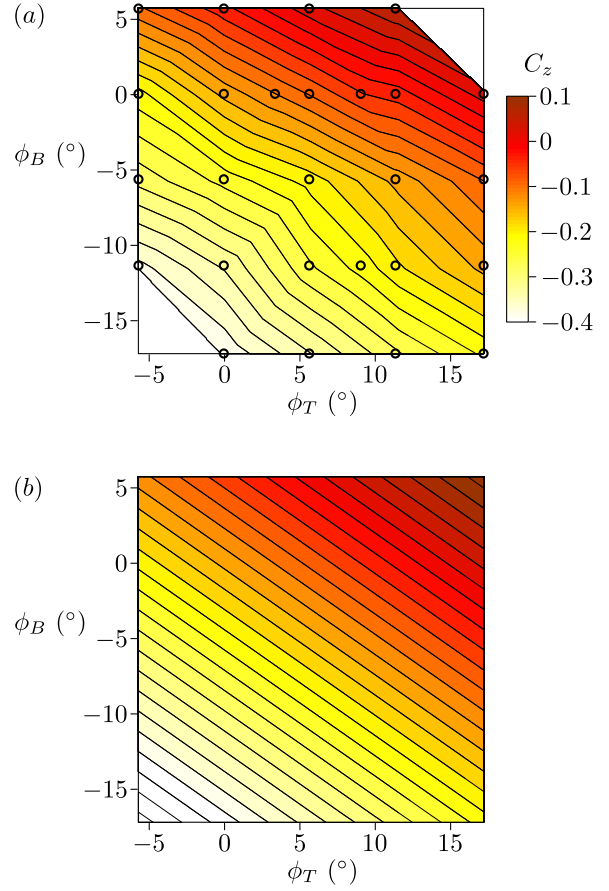


Fig. 12 Lift depending on ϕ_T and ϕ_B : experimental data (a) and affine fit given in Eq. (10) (b). Contour intervals are 0.02.

Eqs. (6) and (9), enable the drag to be expressed as:

$$C_x = C_{x\text{opt}} + \alpha (C_z - C_{z0})^2 + \beta (C_{z0} - C_{z\text{opt}})^2. \quad (11)$$

Since the dependence of C_z and C_{z0} toward ϕ_B and ϕ_T are given in Eqs. (8) and (10), the drag coefficient is then obtained as a function of the top and bottom slant angles. The result is displayed in Fig. 13(b); the drag evaluated from the successive fits is defined as:

$$\begin{aligned} C_x = & 0.248 \\ & - 0.079 \phi_T + 0.062 \phi_B \\ & + 0.400 \phi_T^2 + 0.480 \phi_B^2 \\ & + 0.393 \phi_T \phi_B. \end{aligned} \quad (12)$$

with ϕ_B and ϕ_T in radians. Equation (12) depicts all of the drag trends observed in the experiments. Besides, it is worth noting that the minimum of drag is not particularly sensitive to the angles ϕ_T and ϕ_B : a low value of drag, close to $C_{x\text{opt}}$, can be obtained in a reasonably wide range of parameters around $(\phi_{T\text{opt}}, \phi_{B\text{opt}})$. Finally, the term proportional to $\phi_T \phi_B$ in Eq. (12) corresponds to the coupling effect of the top and bottom

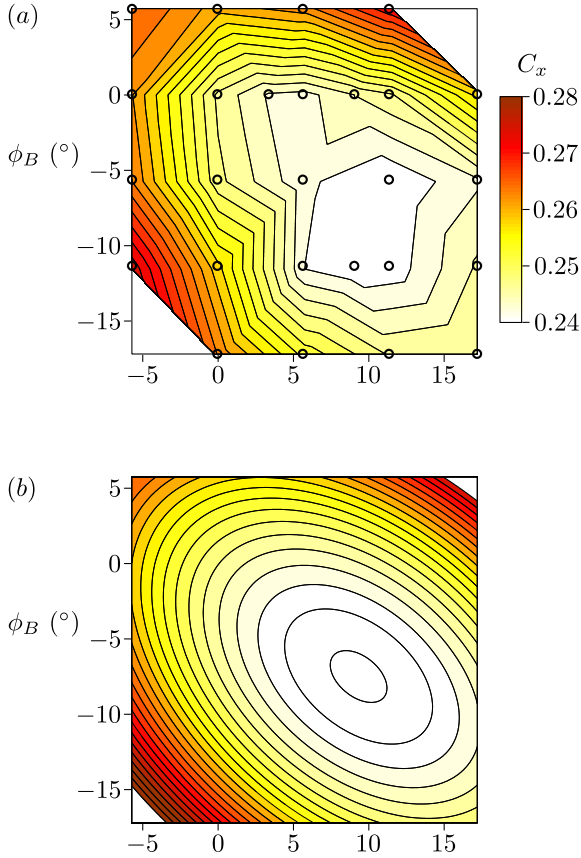


Fig. 13 Drag depending on ϕ_T and ϕ_B : experimental data (a) and law given in Eq. (11) (b). Contour intervals are 0.002.

slant angles. This might be related to the fact that the inclination of the top flap leads to slight variations of pressure on the bottom face as evidenced in Fig. 3(b) and then alters the effect of the bottom flap; reciprocally, the orientation of the bottom flap affects the influence of the top one.

The mechanisms responsible for the selection of the drag and of the lift are then discussed in Sec. 4.

4 Discussion on the drag sources

The quadratic relationship between the drag and the lift is reminiscent of the notions of induced drag commonly used in aeronautics [14]. However, the lift is not the only parameter responsible for the selection of the drag because of the presence of a massive flow separation on the base. Then, as mentioned in Sec. 3.2, the height of the wake seems to have a critical influence, however three-dimensional effects may become dominant over a certain point.

The expression of drag given in Eq. (12) can be rewritten as:

ten as:

$$C_x = 0.248 - 0.079(\phi_T - 0.778\phi_B) \quad (13)$$

$$+ 0.405 C_z^2 \quad (14)$$

$$+ 0.271 \phi_T^2 + 0.182 \phi_B^2. \quad (15)$$

$$(16)$$

with C_z following the affine function defined in Eq. (10) and ϕ_B and ϕ_T in radians. The different terms (13), (14) and (15) may respectively be interpreted as the drag contribution of the wake size, the drag induced by the lift and a local drag induced by the slant angles.

First, the term (13) corresponds to the drag associated with the recirculation region using a bi-dimensional vision. The low pressure in the recirculation region is related to the curvature of the streamlines around the separatrix [15]. This curvature can be evaluated as $(\pi - \phi_T + \phi_B)/L$ with L the recirculation length. In the theoretical limit case ($\phi_T = \pi/2, \phi_B = -\pi/2$) with a flow attached on the flaps, this drag contribution would be nil. One may then expect an expression following:

$$C_{x\,2D} \frac{L_0}{L} \left(1 - \frac{\phi_T - \phi_B}{\pi} \right), \quad (17)$$

with L_0 the recirculation length of the case $\phi_T = \phi_B = 0^\circ$. The values of L for the different slant orientation is not known; yet, assuming $L_0/L \sim 1$, the evaluation of the linear term (13) gives:

$$0.248 \left(1 - \frac{\phi_T - a\phi_B}{b} \right), \quad (18)$$

with $C_{x\,2D} = 0.248$, $a = 0.778 \sim 1$ and $b = 3.14 \sim \pi$. $a \neq 1$ is likely to be an effect of the ground: the bottom flap is less efficient than the top one in orienting the potential flow upstream of the separation. The positive effect of an increase in $\phi_T - a\phi_B$ on drag may then be seen as a transfer of pressure between the wake and the top or bottom face of the geometry. In the case $\phi_T = \phi_B = 0^\circ$, the curvature of the streamlines related to the low pressure region is concentrated near the separatrix of the massive recirculation region. If one of the two flaps is oriented toward the recirculation region, then the flow separates following the flap orientation; it induces some streamline curvature upstream of the base which leads to a decrease in pressure upstream of the oriented flap. Therefore, this phenomenon is directly measured on the lift and explains the affine dependence between C_z and the slant angles. It is important to mention that, in literature, drag reductions are often related to increased mean recirculation lengths past cylindrical shapes [16,17] because the flow orientation at the base separation remains the same whatever the recirculation length is; thus it remains consistent with Eq. (17).

The second term (14) refers to the drag induced by

the lift like in the formalism introduced in aeronautics; in particular, the coefficient 0.405 is expected to be a parameter only dependent on the geometry. This induced drag is associated with the possible presence of strong counter-rotating in the far wake like past the 25° Ahmed geometry.

Eventually, the third term (15) may be interpreted as a local drag induced by the slant angles. As seen in Sec. 3.2, the sides of the flaps are sources of vortices which are responsible for part of the drag. Since these vortices can cancel out after merging, they are not necessarily associated with lift and then may not be taken into account in the term (14).

In Eq. 16, the variations of the drag contributors are of similar magnitude in the studied ranges of angles ϕ_T and ϕ_B . Depending on the configuration, one or two of these sources are negligible; in order to have a global view of these different drag sources, sketches interpreting the flow topology of three configurations are presented in Fig. 14.

Figure 14(a) depicts the case $\phi_T = \phi_B = 0^\circ$. There are no vortices developing from the side edges of the flaps because there is almost no pressure differences between the top (or bottom) and side faces: the term (15) is then close to 0. There is no intense streamwise vortices downstream of the recirculation region either, the lift force is reasonably small: the term (14) is limited. Thus, the main drag source is the massive separation on the base contained in the term (13).

The case $\phi_T = \phi_B \sim 10^\circ$ is displayed in Fig. 14(b). Since $\phi_T - \phi_B \approx 0^\circ$, the term (13) is very close to the previous configuration. In addition, the slant angles are responsible for the development of vortices at the side edges of the flaps, the term (15) is no more negligible. Besides the flaps have constructive effect on the lift so the term (14) is significant. The drag is then increased in comparison to the previous case $\phi_T = \phi_B = 0^\circ$.

Figure 14(c) presents the case $\phi_T \sim 10^\circ$ and $\phi_B \sim -10^\circ$. The comparison of Figs. 4(b) and 8 shows that the height of the wake is strongly reduced compared to $\phi_T = \phi_B = 0^\circ$. The term (13) is then less contributor to the drag. As they have a destructive effects on the lift, the term (14) remains limited. However, each flap is associated with the development of a pair of vortices from their sides which are drag sources and taken into account in the term (15). The total drag is reduced: for moderate slant angles (less than 10° to 15°), the decrease of the term (13) is larger than the local drag generated by the vortices from the flaps. However, when the slant angles are more important (typically over 15°), the drag is increased since the reduction of the wake size do not compensate any more the drag linked to the

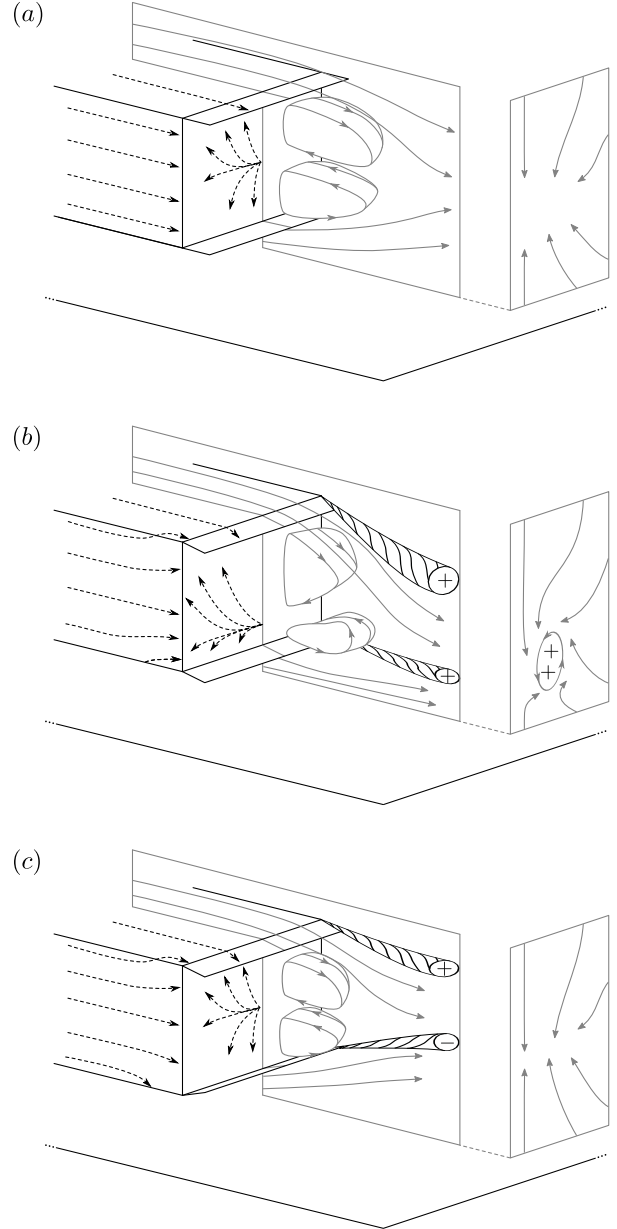


Fig. 14 Sketch of the flow topologies for different configuration: (a), $\phi_T = \phi_B = 0^\circ$; (b), $\phi_T = \phi_B \approx 10^\circ$; (c), $\phi_T = -\phi_B \approx 10^\circ$.

vortices from the corner of the base. Therefore, the competition of these two effect explains the optimal drag configuration for $\phi_T \sim 10^\circ$ and $\phi_B \sim -10^\circ$.

5 Concluding remarks

The inclination of two small flaps downstream of the top and bottom face of the square-back Ahmed geometry [1] is proved to have a critical influence on both drag and lift as well as on the flow topology. When the bottom flap is fixed, the lift and the drag are 1st

and 2nd order polynomial functions of the top flap angle respectively. This leads to a quadratic dependence between the drag and the lift. This drag versus lift relationship is self similar for five different bottom flap angles. In the bi-dimensional domain (ϕ_T, ϕ_B) , the lift is in good agreement with an affine function of ϕ_T and ϕ_B . The drag can be interpolated with a second order polynomial of ϕ_T and ϕ_B adding a term proportional to $\phi_T \phi_B$. This coupling term shows that the optimal top slant angle relies on the bottom flap orientation and the minimum of drag cannot be achieved from independent optimization of the two slant angles.

From these results, a classification of three drag sources is suggested. First, the linear term proportional to $\phi_T - a\phi_B$ quantifies the interest of having a thin wake to limit the base drag. The associated mechanisms may be viewed as a transfer of streamline curvature from the near wake to the top or bottom faces which leads to pressure recovery in the recirculation region. A second term corresponds to a notion of induced drag directly linked to the lift force. However, these two drag contributors are not sufficient to explain the drag results presented in Fig. 13 and a drag contribution associated with the local development of streamwise vortices from the side edges of the flaps is identified.

The presence of terms linked to induced drag points out the interest of having a certain axisymmetry in the recirculation closure. Therefore, the use of additional flaps on the sides is very likely to provide greater drag reductions. Besides, smooth junctions between the flaps would limit the formation of local vortices and then lead to additional drag reduction.

References

1. S. Ahmed, G. Ramm, G. Faitin, Some salient features of the time-averaged ground vehicle wake, Tech. rep., Society of Automotive Engineers, Inc., Warrendale, PA (1984).
2. J. Beaudoin, O. Cadot, J. Aider, K. Gosse, P. Paranthoën, B. Hamelin, M. Tissier, D. Allano, I. Mutabazi, M. Gonzales, et al., Cavitation as a complementary tool for automotive aerodynamics, *Experiments in fluids* 37 (5) (2004) 763–768.
3. P. Gilliéron, A. Kourta, Aerodynamic drag reduction by vertical splitter plates, *Experiments in fluids* 48 (1) (2010) 1–16.
4. J. Beaudoin, J. Aider, Drag and lift reduction of a 3D bluff body using flaps, *Experiments in Fluids* 44 (4) (2008) 491–501.
5. G. Fourrié, L. Keirsbulck, L. Labraga, P. Gilliéron, Bluff-body drag reduction using a deflector, *Experiments in Fluids* 50 (2) (2011) 385–395.
6. G. Pujals, S. Depardon, C. Cossu, Drag reduction of a 3d bluff body using coherent streamwise streaks, *Experiments in fluids* 49 (5) (2010) 1085–1094.
7. C. Bruneau, E. Creuse, D. Depeyras, P. Gilliéron, Active procedures to control the flow past the ahmed body with a 25 rear window, *International Journal of Aerodynamics* 1 (3) (2011) 299–317.
8. B. Khalighi, S. Zhang, C. Koromilas, S. Balkanyi, L. Bernal, G. Iaccarino, P. Moin, Experimental and computational study of unsteady wake flow behind a bluff body with a drag reduction device, SAE paper.
9. C. Bruneau, E. Creusé, D. Depeyras, P. Gilliéron, I. Mortazavi, Coupling active and passive techniques to control the flow past the square back ahmed body, *Computers & Fluids* 39 (10) (2010) 1875–1892.
10. R. Littlewood, M. Passmore, Aerodynamic drag reduction of a simplified squareback vehicle using steady blowing, *Experiments in Fluids* (2012) 1–11.
11. R. Littlewood, M. Passmore, The Optimization of Roof Trailing Edge Geometry of a Simple Square-Back., SAE paper.
12. M. Grandemange, V. Parezanović, M. Gohlke, O. Cadot, On experimental sensitivity analysis of the turbulent wake from an axisymmetric blunt trailing edge, *Physics of fluids* 24 (2012) 035106.
13. M. Onorato, A. Costelli, A. Garrone, Drag measurement through wake analysis, Tech. rep., Society of Automotive Engineers, Inc., Warrendale, PA (1984).
14. G. Batchelor, An introduction to fluid dynamics, Cambridge university press, 2002.
15. D. Riabouchinsky, On steady fluid motions with free surfaces, *Proceedings of the London Mathematical Society* 2 (1) (1921) 206.
16. A. Roshko, Perspectives on bluff body aerodynamics, *Journal of Wind Engineering and Industrial Aerodynamics* 49 (1-3) (1993) 79–100.
17. V. Parezanović, O. Cadot, Experimental sensitivity analysis of the global properties of a 2D turbulent wake, *Journal of Fluid Mechanics* 693 (2012) 115–149.